CFD PREDICTION OF THE TRAJECTORY OF HOT EXHAUST FROM THE FUNNEL OF A NAVAL SHIP IN THE PRESENCE OF SHIP SUPERSTRUCTURE

(DOI No: 10.3940/rina.ijme.2014.a1.269)

R Vijayakumar, S N Singh and V Seshadri, Indian Institute of Technology Delhi, India

SUMMARY

The superstructure of a modern naval ship is fitted with multitude of sensors for electronic surveillance, weapon discharge, navigation, communication and varieties of deck handling equipment. Locating these electronic equipment/sensors and its integration on board is of paramount importance to achieve optimal operational performance of the naval vessel. Among the many problems in locating these sensors (like stability, EMC EMI etc.,), the presence of entrapped hot gases from the ship exhaust affects the functioning of these electronics. Hence the prediction of temperature profile and trajectories of the ship exhaust plume from the funnel around the superstructure during the design stage is a mandatory requirement for positioning the sensors on superstructure. This trajectory prediction is not amenable to theoretical analysis or empirical calculation procedures in the modern warship superstructure. Experimental and CFD studies conducted on ship superstructure are the only reliable tools that are available to estimate temperature field as well as to study the exhaust smoke superstructure interaction on ships. This paper presents the CFD simulation of the published results for two cases, namely hot jet in a cross flow and hot exhaust with a cross flow on a generic frigate. Simulations have been made using k-ε turbulence model with different values of turbulent Schmidt number. It has been observed that temperature field is predicted with reasonable accuracy with turbulent Schmidt number of 0.2.

NOMENCLATURE

V_e	Exhaust velocity, velocity of air injection in the two funnels
V_i	Suction Velocity, velocity of air sucked in the two GT intakes
V_w	Ambient cross flow velocity (m/s), also the relative velocity between the wind and ship
K	Velocity ratio = V_e / V_w
M	Suction to exhaust Mass Ratio.
ψ	Angle of wind relative to the ship's heading
y/w	'y' normalised with respect to funnel width at the base
z/ h	'z' normalised with respect to funnel height
z/ d	'z' normalised with respect to deck height
x/ h	'x' normalized with respect to funnel height
Ts	Temperature of smoke
T_{ambi}	Temperature of ambient air
T_{mes}	Temperature measured at particular location
T_{max}	Exhaust Temperature
θ	Normalised Tempeature rise $\theta = \frac{T_{mes} - T_{ambi}}{T_{max} - T_{ambi}}$
k	Turbulent kinetic energy, m^2/s^2
ε	Turbulent kinetic energy dissipation rate, m^2/s^3
$C_{\xi 1}$, $C_{\xi 2}$	Model constants
α_k, α_ε	Inverse of effective Prandtl number for k and ε
S_k, S_ε	User defined source terms for k and ε.
Sc_t	Turbulent Schmidt number
S_m	Mass added to continuous phase
μ	Molecular viscosity
μ_{eff}	Effective viscosity
μ_t	Turbulent or eddy viscosity
ρ	Density of fluid
σ_k, σ_ε	Prandtl number for k and ε

1. INTRODUCTION

The superstructure of a naval warship is cluttered with weapons, sensors, deck handling equipment/machinery, Gas turbine intake and exhaust. The current practice in naval shipbuilding is to favor short funnels and tall mast to house various electronics and antennas. This results in the problem of smoke nuisance, wherein hot exhaust gases from funnels tend to get trapped in the downwash of the funnel and superstructure and expose various topside operational areas, ventilation openings, electronics and weapon systems to high temperature and contamination. With the use of gas turbines as prime movers in warships, the problem of smoke nuisance has further aggravated with increase in mass flow and higher temperatures of exhaust compared to diesel driven ships. On ships such as aircraft and helicopter carriers, extra care should be taken during design to ensure that the exhaust gas will not interfere with normal operations. The impact of these hot gases has resulted in recurring problems with topside devices like antennas, electronic communication instruments, radar and weapon systems apart from increasing the Infrared signature of the vessel [1,18].

Thus, the prediction of temperature field and the trajectory of the exhaust plume from ship funnel is a vital input for naval architect at the earliest stages of design for positioning and arranging of various topside electronics on a warship. Baham and McCallum [2] have conducted full scale measurements of exhaust plume temperature on board USS Paul F Foster (DD964) vessel and suggested a step by step procedure for estimating the downwind plume gas temperature and trajectories in warship. Warship designers worldwide use these empirical relations for predicting the plume trajectories during initial stages of design to position various equipment in the superstructure. However, the superstructure layout of warship, which houses guns, weapons, electronics etc, has changed considerably over the last century. Kulkarni et al [1], in their review paper describe the evolution of the ship's funnel over the last hundred years and present state of modern warship funnels vis a vis location of superstructure along with various electronics and also discuss various studies on the problem reported by various researchers since 1930's. They also conclude that the use of empirical relation of Baham and McCallum [2] for the modern warship is no longer viable.

In the absence of reliable analytical methods, the designers have to rely upon model experimentation in wind tunnel. Several investigators have conducted isothermal wind tunnel studies to understand various aspects of interaction between exhaust smoke and ship superstructure. Acker [3] has proposed the classic guidelines to avoid downwash based on the wind tunnel studies of model ships. Seshadri and Singh [4] have investigated the problem of smoke ingress into gas turbine intake of naval ships by simulating the phenomenon in a wind tunnel. Kulkarni et al [5-10] have presented the flow visualization studies of the exhaust smoke-superstructure interaction on generic naval ship models.

However the wind tunnel studies are carried out at a relatively advanced stage of design when many aspects of the design are frozen. Making changes at these stages may involve redesigning many aspects of design. Further, wind tunnel studies are very lengthy, time consuming and expensive. It is not possible to cover the entire range of parameters like wind velocity, direction, geometry of the ship structures on the deck, efflux velocity of smoke, yaw angle changes etc. to be simulated in a wind tunnel. CFD has emerged as a serious alternative to wind tunnel studies and is capable of providing solutions early in the design spiral of warships.

In the current design practice, CFD simulation using Reynolds-Averaged Navier-Stokes (RANS) equations are most often used for investigating velocity and temperature field over the superstructure of warships. Therefore there is a need for accurate RANS simulations of interaction between the superstructure cross flow in which, both the prediction of velocity and temperature field are desired. RANS simulation of velocity field and its comparison with the experimental results for simplified warship geometry has been performed by Kulkarni et al[10]. However numerical simulation of temperature contours are relatively few and no systematic study on the choice of the optimum value of turbulent Schmidt number is available. (Turbulent Schmidt number is the ratio of the rate of turbulent diffusivity of momentum to the turbulent diffusivity of heat. It is a measure of relative magnitudes of diffusion of momentum and heat)

Many researchers in other similar fields have experimentally studied a single circular heated jet normally injected into a cross flow. Kamotani and Greber [11] present results on the velocity and temperature trajectories using a heated and unheated air jet in a cross flow, where temperature distribution downstream of the jet was measured using hot wire. They reveal that, there exist distinct temperature and velocity trajectories for heated jets in a cross flow. The plume flow theory for exhaust gases ejected into a uniform, stable crosswind has been subject of a study by Crabb et al [12], Andreopoulos and Rodi [13] as well as Hoult and Weil [14] for application to power plants. The interaction of a heated jet with a deflecting stream has been studied by Ramsay et al [15] who provide insight into the path of heated plume in a cross wind. Chao and Ho [16] used RANS and the standard k–ε model to calculate the temperature field that was experimentally measured by Kamotani and Greber [11], and found no significant changes in the temperature contour patterns when turbulent Schmidt numbers ranging from 0.5 to 0.9 were used. Guangbin et al [17], in their numerical simulation of jet in a confined cross flow recommend a constant Schmidt number of 0.2 in predicting turbulent scalar fields in heated jet-in-crossflow using RANS solver. However the numerical investigation has been carried out for the velocity ratios in the range 5 to 9, whereas ships operate at velocity ratios less than two. Vijayakumar [18] in his PhD thesis illustrates the interaction of hot exhaust gas from funnel and its interaction on intake and superstructure on generic naval frigates. This phenomenon is also relevant to other ship types, such as: cruise ships and passenger vessels where the passengers have access to the deck.

Traditionally, a constant Schmidt number of approximately 0.85 has been used to predict the temperature fields in turbulent flows. The objective of the present work is to evaluate the value of Schmidt number that is most suitable for predicting temperature contours for velocity ratios in the range 1 to 2. For this, a series of RANS simulations, using turbulent Schmidt number varying from 0.1 to 0.85 for two cases are performed, wherein turbulent closure is provided by standard k-ε model. The flow configurations used in the present work are as follows:

(a) Case A: A round fully developed turbulent jet discharging normally into a uniform cross flow in a rectangular wind tunnel (Figure 1), experimentally investigated by Ramsay et al[15] is used for validating numerical model

(b) Case B: A hot exhaust from funnel ejecting in the turbulent wake of the simplified superstructure of a generic frigate model in a wind tunnel (Figure 2) which is experimentally investigated by Vijayakumar et al [19] is used to validate the numerical simulations.

2. COMPUTATIONAL APPROACH

2.1 GOVERNING EQUATIONS

For a variable density incompressible steady flow with constant viscosity, the Reynolds Averaged Navier Stokes (RANS) in integral form for mass, momentum and energy can be written in the following general form:

$$\frac{\partial}{\partial t}\int\int_{Q}\int(\rho\varphi)\,dQ+\int\int_{A}\rho\varphi\overline{V}\,d\,\overline{A}$$

$$=\int\int_{A}\Gamma_{\varphi}\nabla\varphi\,d\,\overline{A}+\int\int_{Q}\int S_{\varphi}\,dQ \tag{1}$$

Where, φ is a variable, which can take values

- 1 to give the continuity equation
- u,v,w to give the momentum equation in three direction
- h to give the energy equation

The flow field domain (solution domain) is subdivided into finite number of control volumes (CV). The conservation equations, the general form of which is given in Eqn. 1, are then applied to each control volume. In actual implementation this integral equation is converted into linearised algebraic difference form (Eqn. 2) for the discrete dependent variable and applied to the computational node positioned at the centroid of each control volume. The general conservation equation in difference form can be written as

$$\frac{(\rho\phi_p)^{t+\Delta t}-(\rho\phi_p)^{t}}{\Delta t}\Delta Q+\sum_{f}^{N_{faces}}\rho_f\overline{v}_f\phi_f.\overline{A}_f=\sum_{f}^{N_{faces}}\Gamma_{\phi}(\nabla\phi)_n.\overline{A}_f+S_{\phi}Q \tag{2}$$

Interpolation is used to express variable values at the control volume (CV) surface in terms of CV-center node values. The standard k-ε model which is a semi empirical model based on equations for turbulent kinetic energy (k) and its dissipation rate (ε), is then used. The transport equations are

$$\overline{U_i}\frac{\partial k}{\partial x_i}=-\overline{u_i^{'}u_j^{'}}\frac{\partial\overline{U}}{\partial x_j}-\varepsilon+\frac{\partial}{\partial x_i}\left[\frac{\nu_t}{\sigma_k}\frac{\partial k}{\partial x_i}\right] \tag{3}$$

$$\overline{U_i}\frac{\partial\varepsilon}{\partial x_i}=-C_{\varepsilon1}\frac{\varepsilon}{k}\overline{u_i^{'}u_j^{'}}\frac{\partial\overline{U}}{\partial x_j}-C_{\varepsilon2}\frac{\varepsilon^2}{k}+\frac{\partial}{\partial x_i}\left[\frac{\nu_t}{\sigma_\varepsilon}\frac{\partial\varepsilon}{\partial x_i}\right] \tag{4}$$

where σ_k=1.0 , $C_{\xi1}$=1.44, $C_{\xi2}$=1.92 σ_k=turbulent Prandtl number for k (1.0) and σ_ε=turbulent Prandtl number for ε (1.3). These are the default constants for the standard k-ε model. The eddy or turbulent viscosity, ν_t is computed by combining k and ε as follows

$$\nu_t=\rho C_\mu\frac{k^2}{\varepsilon}\qquad\text{where } C_\mu=\text{constant (0.09)} \tag{5}$$

The time averaged thermal equation is modeled as:

$$\frac{\partial\overline{T}}{\partial t}+u_i\frac{\partial\overline{T}}{\partial x_i}=\frac{\partial}{\partial x_i}\left(\alpha\frac{\partial\overline{T}}{\partial x_i}-\overline{u_i^{'}T^{'}}\right)+S \tag{6}$$

Where T is the temperature and S source term. The turbulent heat transport is also assumed to be related to gradient of transport quantity:

$$-\overline{u_i^{'}T^{'}}=\alpha_t\frac{\partial\overline{T}}{\partial x_i} \tag{7}$$

Where α_t=(ν_t/ Sc_t) is the turbulent diffusivity of heated mass and Sc_t is called turbulent Schmidt number.

2.2 FLOW CONFIGURATION AND DOMAIN

2.2 (a) Case A

Three sets of CFD simulations for which the corresponding experimental data is available in literature [15] for five Sc_t values in the range 0.1 to 0.85 are executed. Table 1 shows the boundary conditions applied for the heated jet and cross flow in the CFD simulation for the three cases.

The computational domain, coordinate system along with boundary conditions is described in Figure. 1. The jet diameter D is chosen same as the experimental set up i.e 2.35cm. The jet center is located at 6D downstream of the cross flow inlet, which ensures that the inlet boundary condition has negligible effect on the computed flow field. The wind tunnel exit is at 29D downstream of the jet to eliminate unwanted interference from the downstream boundary. The domain size in span wise and the vertical direction are 8D and 12D respectively. The boundary conditions applied to the computational domain are as follows (They are also shown in Figure 1(a)):

(a) At the inlet of the jet. **INLET** boundary condition is specified to represent the velocity V_j and the temperature T_j as indicated in Table 1. In order to create the fully developed flow profile at the exit of the jet, user defined function (udf) programme was created and imported into Fluent.

(b) At the entry of the computational domain, the **INLET** boundary condition is specified to represent velocity of cross wind V_w and ambient temperature T_a as indicated in Table 1.

(c) Since the sides of the computational domain, are to be compared with the wind tunnel experimental data, a no-slip, adiabatic **WALL** boundary condition, as applicable to the wind tunnel is applied at these walls.

(d) At the exit of the computational domain, the **OUTLET** boundary condition is applied.

2.2.(b) Case B

The generic frigate model used for the experimental investigation [19] is shown in Figure 2(a). The naval ships with displacement of over 3000 tons usually have two engine rooms spaced sufficiently apart in its general arrangement, necessitating two separate funnels and intakes. Further, the modern frigate type ships indicate that they are fitted with two plated masts to accommodate various antennas/radars at different levels and they are located close to funnels. The funnels and masts are of trapezoidal shape rather than aerodynamic, to reduce radar cross section of the vessel. The model in the experimental investigation [19] represents generic frigate with two masts where the forward mast is located over the bridge and two funnels and two intakes are located near the base of the funnel. The typical dimensions of deck height and free board of a naval ship and the dimensions of the representative superstructure of generic frigate are shown in Figure 2(a).

The computational domain along with boundary conditions is shown in Figures 2(b) & (c). The superstructure configurations are modeled with the computational domain extending up to five times the ship length (between upstream and down stream) in the ship moving direction (Global x axis in this analysis), three times the breadth transverse (y direction) and three times the funnel height vertically (z direction). The mesh is extended up to 23.5 cm on port and starboard side of the model. The upstream edge of the computational domain extends upto one length of the model from the forward edge of the superstructure (to ensure that it is greater than 3 times the height of the superstructure which is 24 cm). The downstream edge of the computational domain extends up to three times the length from the aft end of the superstructure (to provide for the path of the plume to fully develop). The boundary conditions applied to the computational domain are as follows (They are also shown in Figure.2):

(a) At the entry of the computational domain, the **INLET** boundary condition is specified to represent velocity of cross wind V_w as indicated in Table 2.

(b) Since the sides of the computation domain, it is to be compared with the wind tunnel experimental data, a no-slip, adiabatic **WALL** boundary condition, as applicable to the wind tunnel is applied.

(c) At the exit of the domain, the **OUTLET** boundary condition is applied.

(d) And on the superstructure configuration (Figure 2 (b)), at the funnel exit, the **INLET** boundary condition is imposed for the air with a velocity V_e as indicated in Table 2.

(e) At the GT suction intakes, the **INLET** boundary condition is imposed for the air with a velocity $-V_i$ as indicated in Table 1 has been applied. Rest of the model is assigned as WALL boundary condition.

(f) Finally, on the Bottom of the domain and on the superstructure model, no-slip, adiabatic WALL boundary condition is applied.

2.3 MESH GENERATION

The computational domain and its discritisation using the 3D hexahedral structured mesh have been carried out using GAMBIT version 2. by creating journal file. The mesh is generated such that the mesh quality criteria (in terms of the skewness, orthogonality and warpage) specified in FLUENT is satisfied for both the cases. For both the cases, the discritisation was achieved in two stages. In the first stage, the computational domain is divided into various zones. Each zone has been discritised with the hexagonal structured grid, which can be varied independently. The grid resolution and density has been varied for various zones in the computational domain and solved for the flow pattern and plume path. However, the inter zone face mesh compatibility limits the variation of grid size from one zone to another. (1.25% increase in cell size from one zone to another). In order to get much more accurate matching of velocity contours, a second stage of grid adaptation has been employed. In the second stage, the mesh is adapted based on the plume velocity and temperature gradients as well as the gradients of flow parameters in the wake region. Such a solution-adaptive grid capability is particularly useful for accurately predicting flow fields in regions with large gradients. Solution-adaptive refinement makes it easier to perform grid refinement studies and reduces the computational effort required to achieve a desired level of accuracy, since mesh refinement is limited to those regions where greater mesh resolution is needed. The procedure of mesh refinement is described in following section.

2.4 GRID ADAPTATION

A reasonably well-converged solution using a relatively fine mesh is obtained before performing an adaptation where in the mesh is further refined to capture velocity and temperature profile accurately. For Case A one such grid adaptation undertaken is shown in Figure 3. The initial coarse mesh with 251,073 tetrahedral cells is used to obtain the initial solution. This coarse mesh in the centerline plane of symmetry of the computational domain is shown in Figure 3 (e). Thereafter, for adaptation, the regions of pressure deficit are identified from the plot of total pressure (shown in Figure. 3 (a)). The regions of increased velocity in the region of the jet are identified from the plot of total velocity (shown in Figure 3 (b)) and the regions of temperature gradient in the jet are identified from the plot of total temperature(shown in Figure 3 (c)). The iso-values of pressure, velocity and temperature thus identified are used to refine the mesh in the wake region as well as in the region of the jet. The resulting mesh, after smoothing and swapping, in the centerline plane of symmetry of the computational domain is shown in Figure 3 (f). It can be seen that the interface between the refined region within the jet & the wake and the surrounding mesh is not sharp. The adapted mesh now has 511,482 tetrahedral cells, an increase of 260,309 cells in the region of interest and almost a 2-fold increase in the total number of cells. The resulting mesh is optimal for the flow solution because the solution based on a coarse mesh is used to determine where additional cells are added. Further, the effect of mesh refinement on the solution can be studied without completely regenerating the mesh. The analysis was performed using commercial package (FLUENT V6) using segregated implicit RANS solver with standard k-ε turbulence model. A hybrid differencing scheme has been employed to discritize the energy equation. First order upwind differencing scheme is used for initial 100 iterations to initialize the value of temperature, pressure, momentum and the turbulence viscosity discretization at the nodes and the second order upwind differencing scheme was employed till solution is converged. The residual convergence for different iterations is shown in Figure 3 (d), where A represents, solution of 100 iterations with first order upwind differencing scheme, B represents converged solution using second order upwind differencing scheme with pressure adaption. C and D in the figure represent the solution convergence with velocity and temperature adaptation.

Similarly for Case B, the flow around the superstructure contains flow features that are easy to identify. For instance, wakes represent a total pressure deficit, and jets are identifiable by a region of relatively high-velocity. The iso-value grid adaptation feature of FLUENT using the parameters of pressure and velocity is used to adapt the grid. It is best for both accuracy and convergence to have a mesh in which the changes in cell volume are gradual. The grid created after the adaptation process results in a mesh that does not have this property. The grid is therefore improved by using volume adaptation wherein the refining is based on either the cell volume or the change in volume between the cell and its neighbors.

One such grid adaptation undertaken is shown in Figure 4. The initial coarse mesh with 711,291 tetrahedral cells is used to obtain the initial solution. This coarse mesh on the centerline plane of symmetry of the computational domain is shown in Figure. 4 (c). Thereafter, the regions of pressure deficit are identified from the plot of total pressure (shown in Figure. 4 (a)) and the regions of increased velocity in the region of the jet is identified from the plot of total velocity (shown in Figure. 4 (b)). The iso-values of pressure and velocity thus identified are used to refine the mesh in the wake region as well as in the region of the exhaust jet. To improve the mesh, it is refined using volume adaptation with the criterion that the maximum cell volume change should be less than 50%. The minimum cell volume for adaptation is also chosen. The resulting mesh, after smoothing and swapping, in the centerline plane of symmetry of the computational domain is shown in Figure. 4(d). It can be seen that the interface between the refined region within the jet & the wake and the surrounding mesh is not sharp. The adapted mesh now has 1,312,319 tetrahedral cells, an increase of 601,100 cells in the region of interest and almost a 2-fold increase in the total number of cells. The effect of mesh refinement on the solution can be studied without completely regenerating the mesh.

The solution from the previous (coarse) mesh is mapped on to this new (adapted) mesh and the calculations are re-started. The analysis is performed using commercial package (FLUENT V6) using segregated implicit RANS solver with standard k-ε turbulence model as described earlier. The procedure uses structured meshing for discretisation with hexagonal cells. The solution process requires iterations with check on the residuals on the right hand side of the governing equations. This iterative procedure is continued till convergence. Residual convergence (Figure 6) shows the convergence histories of the residuals for the momentum (u, v, w) in the x-, y- and z directions, continuity, turbulent kinetic energy, dissipation rate and energy. These provide a global measurement of error both in conservation of mass momentum and energy. The residual limit is set to a value below 10^{-6}. The converged solution is carefully post processed for analysis and the results are presented in the subsequent sections.

3. RESULTS AND DISCUSSIONS

3.1 COMPARISION WITH THE EXPERIMENTAL MEASUREMENTS OF RAMSAY ET AL [15] - CASE A

The experimental temperature contours that are available for three cross section planes are compared with the CFD simulation for the various values of the Sc_t. The iso-temperature plots are made in terms of dimensionless parameter Θ defined as $\Theta = (T-T_{ambi})/(T_{max}-T_{ambi})$. The difference between the experimental and the computed values of non dimensionalised Θ are calculated for the corresponding experimental points. The percentage of error between the experimental measurements and the CFD simulation is thereafter calculated at each plane by using the Eqn. 6 and is presented in Table 3.

Percentage of error on each plane

$$= \sqrt{\frac{1}{n}\sum_{i=1}^{n}\left[\theta_{\exp} - \theta_{cfd}\right]^2} \tag{8}$$

Where,
$\theta_{\exp}$ = Normalised temperature from experiments
θ_{CFD} = Normalised temperature from CFD
n = number of data points

3.1(a) Case A1: Momentum Ratio of 2.0

Turbulent Schmidt numbers in the range of 0.1 to 0.85 were tested to study the effect of the Sc_t number for predicting the hot jet mixing in the cross flow for the case of momentum ratio MR=2. Figure 5 exhibits a quantitative comparison of the CFD simulated temperature contours with experimental measurements for three planes. Figures 5 (a), (b) and (c) present experimental results of iso-temperature distribution at planes x/d=1.87, 3.56 and 5.48 respectively and Figures 6 (d) to (r) are numerical results for various turbulent Schmidt numbers for the 3 planes. These results indicate that the temperature contours become concentrated with increasing turbulent Schmidt's number For example the contour line of Θ=0.1 was predicted to be at the y value of 0.5-2.9D at center line of plane x/d=1.87 when the Sc_t of 0.85(Figure 5(d)) was used, while the location of contour line of Θ =0.1 extends to y=0.25 (Figure 5(e)) when a Sc_t of 0.2 is used. Similarly concentration of contours are also seen for the planes x/d=3.56 and 5.48 when higher Sc_t number are used. From the CFD prediction it is found that, the predicted temperature contours are found to be quite sensitive to the Sc_t number. The temperature contours at three planes at Sc_t of 0.85 shows the values are over predicted. Table 3 shows the percentage of errors between the experimental and predicted results for various Sc_t numbers. The percentage of error is least for turbulent Schmidt number of 0.2 and it agrees with the experimental data reasonably well.

3.1 (b) Case A2: Momentum Ratio of 1.0

Similar to MR 2, the effect of Sc_t number has been numerically simulated for MR=1. Figure 6 shows a quantitative comparison of the CFD simulated temperature contours with experimental measurements for the three planes. Figures 6.(a), (b) and (c) present the experimental results of iso-temperature distribution at planes x/d=1.87, 3.56 and 5.48 respectively and Figures 6 (d) to (r) are numerical results for various Sc_t. Similar to the case of the Momentum ratio of 2.0, the numerical prediction using Schmidt's numbers of 0.85 to 0.3 tend to concentrate and over predict the temperature for all the three planes (Figures 6 (d) to (l)). The near wall prediction of the temperature at all Sc_t is not accurate. Generally Sc_t value of 0.2 gives the best agreement with least percentage of error (Table 3).

3.1 (c) Case A 3: Momentum Ratio of 0.1

CFD validation for low momentum ratio of 0.1 was also carried out. The experimental and CFD comparison for the constant temperature contours are shown in Figure 7. As in the case of momentum ratios of 1 and 2, the numerical prediction using higher turbulent Schmidt's numbers tend to over predict the temperature values. The near wall prediction of the temperature for all Sc_t is not adequate and the turbulent Schmidt's number of 0.2 still gives the best agreement with least error.

3.2 COMPARISION WITH THE MEASUREMENT OF VIJAYAKUMAR ET AL [19] - CASE B

The computational simulations so far have shown that with a constant Sc_t number of 0.2 the results match reasonably well with the experimental results for all the three momentum ratios temperature prediction. CFD simulation for the experimental data presented by Vijaykumar et al [19] for generic naval frigate has also been carried out. Five values of Sc_t were tested to study the effect of the Sc_t number on predicting of the temperature field.

The comparison of experimental [19] and CFD results (four Sc_t - 0.85, 0.4, 0.2 and 0.1) for the flow condition with cross wind, with hot air injection through funnel and suction through intakes for the 4 planes are presented in Figures 8 and 9. The percentage of errors by CFD prediction with respect to experimental data have been given in Table 4.

The experimentally measured iso-temperature contours of Θ for Plane 1 are given in Figure 8(a) and the CFD results of Θ for various Sc_t are given in Figure 9(b) to (e). The numerical prediction using Schmidt's number 0.85 and 0.4 tend to concentrate and over predict the temperature for this plane. The experimentally measured Θ_{max} is 0.25 at Plane 1, while the CFD prediction of Θ_{max} is 0.34(S_{ct}=0.85), 0.28(S_{ct}=0.4) 0.26(S_{ct}=0.2).and 0.095(S_{ct}=0.1). The numerical prediction using constant turbulent Schmidt's number of 0.2 is more accurate with least error.

At Plane 2, which is located half the funnel height distance from the forward funnel, similar trend as in case of Plane 3 are observed with the CFD prediction using various Sc_t numbers. Even though the Plane 4 is located close to the funnel, the Θ_{max} is 0.11 at this plane, mainly due to the path of the plume, which is more directed towards forward mast. (Figure 8(b)) before reaching Plane 4. The Θ_{max} by CFD prediction are 0.15 (S_{ct}=0.85), 0.13(S_{ct}=0.4), 0.12(S_{ct}=0.2). and 0.065 (S_{ct}=0.1) for various Schmidt's number. Even though the variation of Θ_{max} is not much with higher Schmidt's number (0.85, 0.4) the constant Sc_t number of 0.2 is more accurate with least error.

The iso temperature contours from aft funnel at planes 8 and 9 are given in Figure 10. On comparing the experimental and CFD prediction for these planes, it is again found that generally the Sc_t number of 0.2 gives the best agreement with least error (Table.4).

Figure 10 shows the iso temperature contours of Θ on the centerline plane for four turbulent Schmidt's number (0.2,0.4,0.6 and 0.85) at K=1, Te=350 K, M=1 and Ta=300 K and yaw angle at 0^o.These results indicate that the temperature profiles become longer with increasing Sc_t number. For example, the contour line of Θ=0.05 was predicted to be x/h≅2.5 downstream of the aft funnel when Sc_t number of 0.2 was used (Figure 10(a)), while as shown in Figure 10(b), the location of contour line extended even up to aft mast when a Sc_t number of 0.4 is used. The average raise in temperature at forward intake is measured as 3^o greater than the ambient temperature. The predicted values of intake temperature raise are 3.06, 4.12, 4.5 and 5 for Sc_t numbers of 0.2, 0.4, 0.6 and 0.85 respectively. Thus the hot plume-mixing rate was found to be quite sensitive to Sc_t number. In fact, when the Sc_t number is greater than 0.2, the agreement between the experimental results with the predicted values becomes poor.

The deviations between the measured and the computed values of normalized Θ for hot exhaust are given in Table 4. The error percentage varies between 9.1% to 3.34% using constant Sc_t number of 0.2, which is least in comparison with the other Sc_t numbers. Hence, constant Sc_t number of 0.2 is most suitable for hot exhaust gases prediction.

4. CONCLUDING REMARKS

(a) The comparison of iso- temperature contours from CFD prediction with those of published experimental results of jet in cross flow for three momentum ratios of 0.1, 1.0 and 2.0 show good agreement for all the three planes by using a constant Sc_t of 0.2.

(b) Similarly, the CFD prediction of iso temperature contours using the constant Sc_t number of 0.2 for the flow over the simplified superstructure with heated exhaust agrees well with the experimental data for all the four planes.

(c) It can also be concluded that the grid refinement and grid adaptation techniques adopted provide satisfactory results. In view of the reasonably good agreement with experimental results, the degree of grid refinement may be considered to be adequate.

(d) The CFD simulations using the standard k-ε model with Sc_t 0.2 are able to predict the temperature and velocity profile for wide range of velocity ratios. Further the numerical simulations give much more detailed and accurate temperature profile predictions as compared to the existing empirical relations.

5. REFERENCE

1. KULKARNI PR, SINGH SN, SESHADRI V The Smoke Nuisance Problem On Ships - A Review", *Journal of Maritime Engineering*, Vol. 147, Part A2 2005, pp. 27-50.
2. BAHAM GARY J. AND D MC CULLUM, "Stack Design Technology for Naval and Merchant Ships", *trans SNAME, Vol 85*, *pp 324-349*, 1977
3. ACKER, H.G., "Stack Design to Avoid Smoke Nuisance," *Transaction SNAME, Vol. 60, pp566-594*, 1952.
4. SESHADRI V, SINGH SN, KULKARNI *PR* "Study of Problem of Exhaust Smoke Ingress into GT intakes of a Naval Ship" *Journal of Ship Technology, Vol 2, NO1, pp22-35*, Jan 2006
5. KULKARNI PR, SINGH SN, SESHADRI V "Flow Visualisation Studies of Exhaust Smoke-Superstructure Interaction on Naval Ships" *Naval Engineers Journal (NEJ) Vol. 117, No. 1, Winter 2005, ASNE (American Society of Naval Engineers)*
6. KULKARNI PR, SINGH SN, SESHADRI V "Experimental Study Of The Flow Field Over Simplified Superstructure Of A Ship", *International Journal Of Maritime Engineering*, *Vol. 147, Part A3* in 2005.
7. KULKARNI PR, SINGH SN, SESHADRI V "Parametric Studies of Exhaust Smoke Superstructure Interaction on a Naval Ship Using CFD", *Computers and Fluids ,Vol .36 ,pp 794-816,* 2007
8. KULKARNI PR, SINGH SN, SESHADRI V "Behavior of Exhaust Gases in the Wake of a Bluff Body" *Int. Conference "MARINE CFD 2005", RINA (Royal Institution of Naval Architects) at Southampton, UK* ,30-31 March 2005
9. KULKARNI PR, SINGH SN, SESHADRI V "Comparison of CFD Simulation of Exhaust Smoke- Superstructure Interaction on a Ship with Experimental Data" *Naval Platform Technology Seminar-2005 (NPTS 05), Singapore on* 17-18 May 2005.
10. YASUHIRO KAMATONI AND ISSAC GREBER "Experiments on a turbulent jet in a Cross Flow" *AIAA Journal Vol 10*, *pp1425-1429,* 1972.
11. CRABB D, DURAO D.F.G, WHITELAW J H, A round jet normal to a crossflow, *Transaction of the ASME. Journel of fluid engineering* 103 (1981)142-153
12. ANDREOPOULOS J, RODI W, Experimental investigation of jets in a crossflow, *Journal of fluid Mechanics 138*, *pp 93-127,* 1984
13. HOULT AND WEIL, "Turbulent plume in Laminar Crossflow", *Atmospheric Environment, 6, pp 513-530,* 1972
14. RAMSAY JW AND GOLDSTEIN RJ "Interaction of heated jet with deflecting stream" NASA, 1970
15. Y-C. CHAO AND W-C. HO "Heterogeneous and non-isothermal mixing of a lateral jet with a

swirling crossflow" *Journal of Thermophysics, 5, pp. 394–400* (1990)

16. GUANGBIN HE, YANHU GUO, ANDREW T H "The effect of Schmidt number on turbulent scalar mixing in a jet-in-crossflow" *International Journal of Heat and Mass Transfer 42, pp 3727-3738,* 1999.
17. VIJAYAKUMAR R "A Study on the interaction of exhaust smoke with the superstructure and gas turbine intakes of naval ships" *Ph D Thesis, IIT Delhi* 2009
18. VIJAYAKUMAR R, SESHADRI V, SINGH SN, KULKARNI PR "A Wind Tunnel Study on the Interaction of Hot Exhaust from the Funnel with the Superstructure of a Naval ships" *Oceans 2008, Kobe, Japan,* 18-21 April 2008

Table 1 Boundary Conditions used in the CFD Simulations (Heated Jet in a Cross Flow) for validation with Experimental Results [15] - Case A

CFD simulation no	Momentum ratio	Velocity ratio	Boundary Conditions					
			Inlet (Cross flow)			inlet (Jet)		
	MR	K	V_w	T_a	ρ_w	V_j	T_j	ρ_j
			m/sec	K	kg/m^3	m/sec	K	kg/m^3
1	2	2.4	30	295	1.19	71.18	350	1.007
2	1	1.2	30	295	1.19	35.59	350	1.007
3	0.1	0.12	60	295	1.19	7.237	350	1.007

Table 2: Boundary Conditions used in CFD simulations of Heated Exhaust Plume for Simplified Generic Superstructure Model. [19] - Case B

	Velocity m/sec	Temperature Kelvin	mass balance fraction
Cross wind	$V_{w=}10$	T_a =295	----
Forward and aft plume gas	V_e =10	T_e =350	----
Forward and aft intake	--	--	1.0 (with respect to exhaust)
Outflow	--	--	1.0(with respect to cross wind)

Table 3: Average Percentage Deviations between the Experimental [15] and the Computed Values of θ for various Sc_t (Case A).

CFD Simulation	Planes	Error percentage for various Sc_t				
MR	X/D	0.85	0.6	0.3	0.2	0.1
2.0	1.87	11.02	9.38	7.51	6.61	6.66
	3.56	11.94	7.01	6.36	6.12	6.37
	5.48	8.65	7.42	6.44	6.04	4.96
1.0	1.87	14.46	13.59	11.46	9.50	11.71
	3.56	12.42	10.23	5.87	4.38	6.37
	5.48	11.425	9.2	5.17	3.69	4.96
0.10	1.87	11.43	9.08	5.59	5.96	9.68
	3.56	9.01	8.19	6.61	5.74	6.07
	5.48	11.08	9.18	5.95	4.67	5.02

Table 4: Percentage Deviators between the Experimental and the Computed Values of θ for various Sc_t (Case B).

CFD Simulation	Planes	Error percentage for various Turbulent Schmidt's number			
		0.85	**0.4**	**0.2**	**0.1**
Forward Flume	Plane 1	10.4	8.95	3.34	5.68
	Plane 2	8.65	7.76	6.76	7.08
Aft Flume	Plane 3	14.14	8.16	9.10	14.52
	Plane 4	9.37	4.51	3.40	7.79

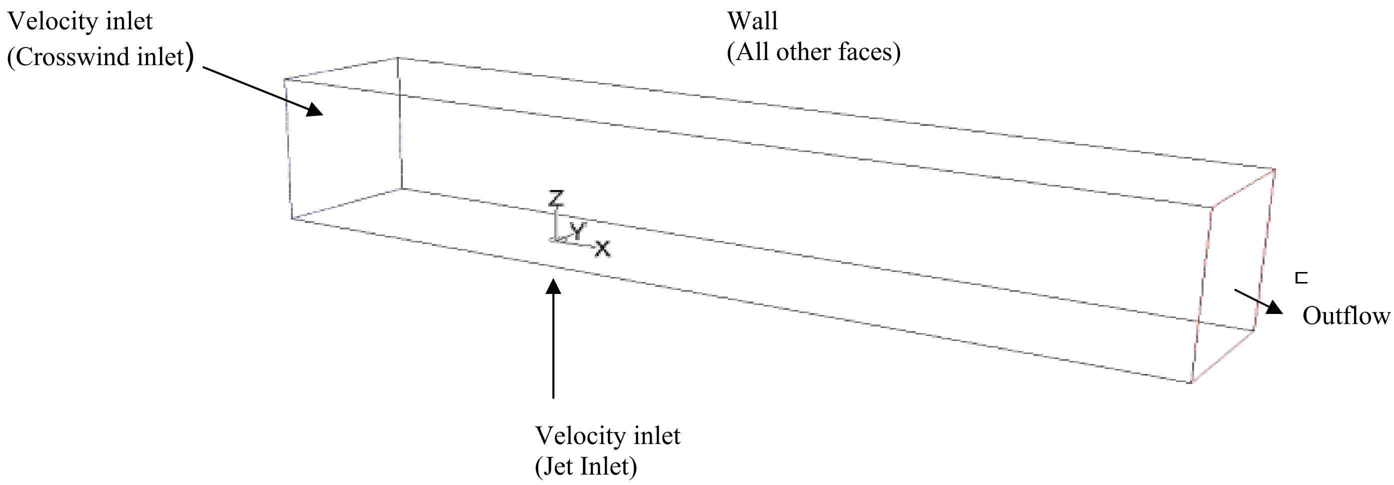

(a) Boundary conditions for heated jet in a cross flow

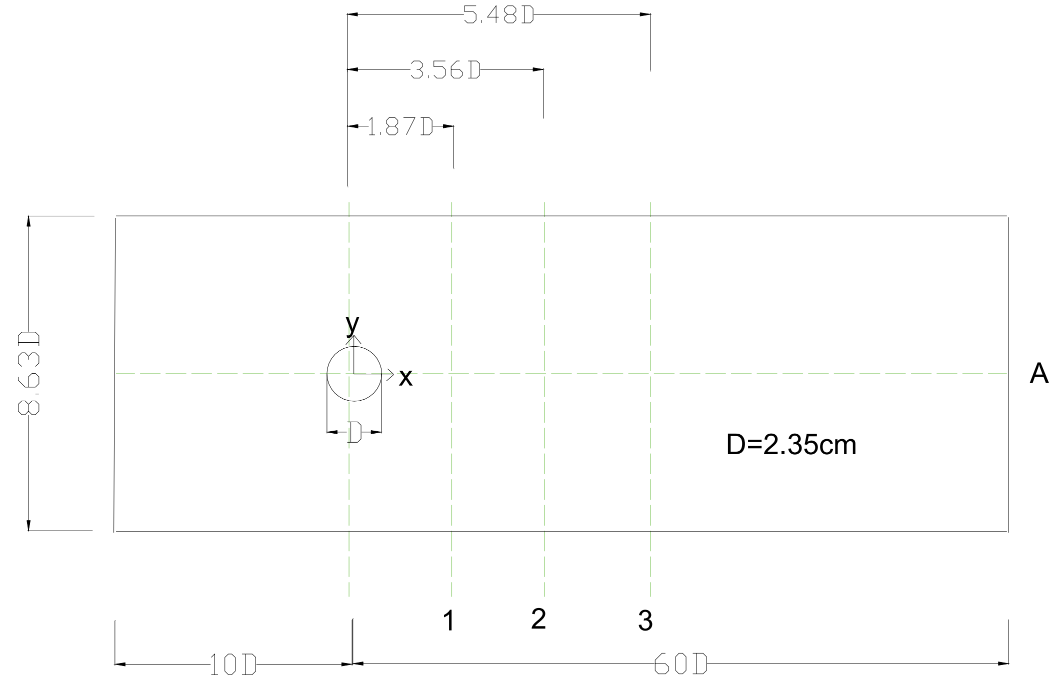

(b) Location of three comparison planes along with axis in the plan view of jet in cross flow.

Figure 1 Flow Configuration, boundary conditions and measurement plane for the jet in a cross flow case A[15]

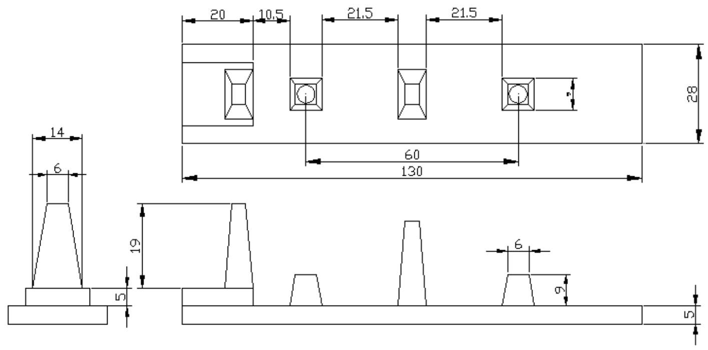

(a) Dimensions of the representative superstructure of Generic Frigate model[19]

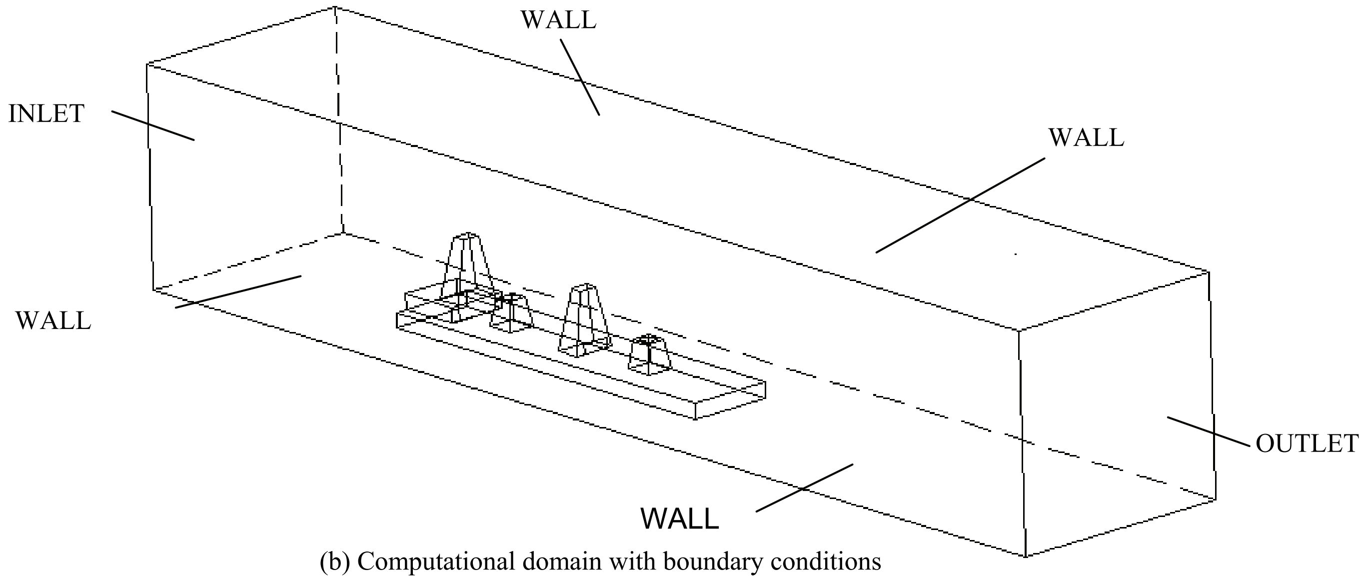

(b) Computational domain with boundary conditions

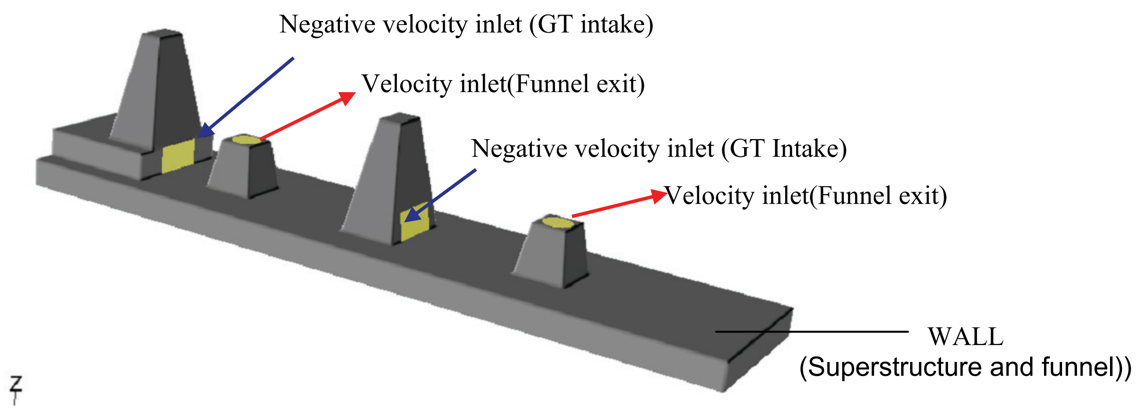

(c) Boundary conditions on the Model

Figure 2 Flow Configuration and boundary conditions for simplified superstructure of a Naval Ships[19]

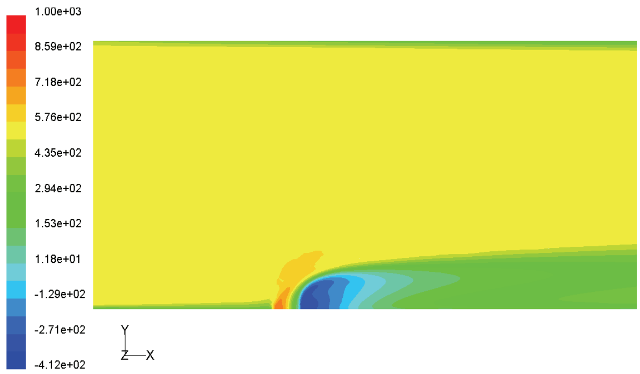

(a) Contours of total Pressure(Pa)

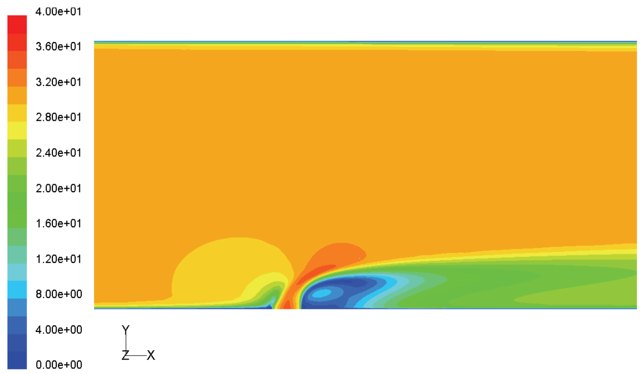

(b) Contours of Velocity (m/sec)

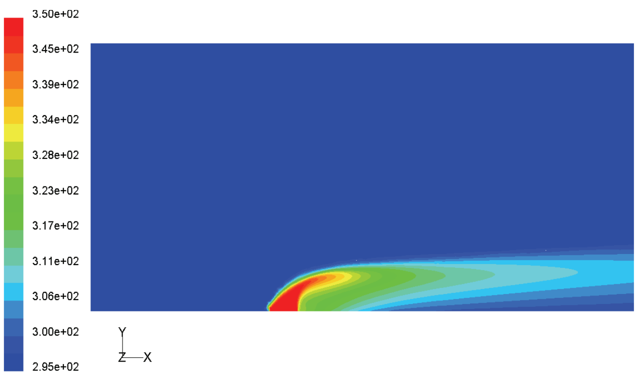

(c) Contours of total Temperature(^{o}K)

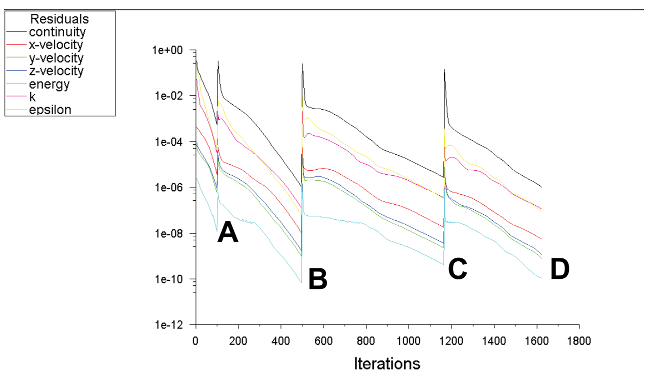

(d) Residuals for different Iteration

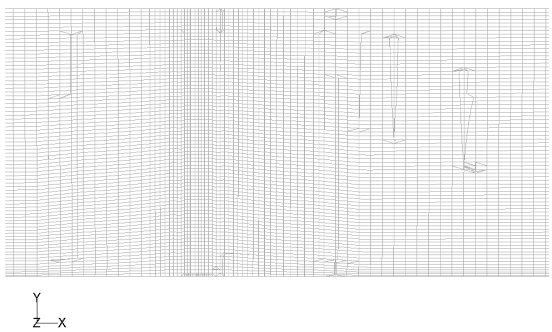

(e) Coarse mesh with 251,073cells

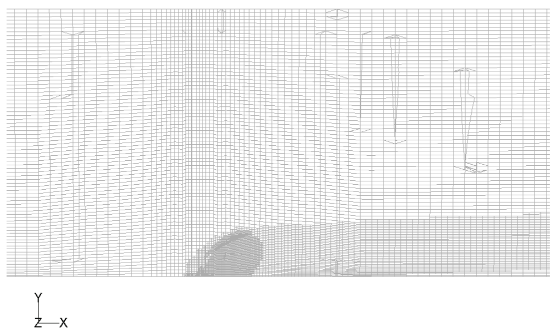

(f) Adapted and refined mesh with 511,482cells

Figure 3: Details of Computation in the Centerline Plane for jet in a cross flow at MR =1 (Case A)

(a) Plot of total pressure on centerline plane

(b) Plot of velocity magnitude in the centerline plane

(c) Coarse mesh with 711,291 cells

(d) Adapted and refined mesh with 1,312,319 cells

Figure. 4: Grid Adaptation Details for the Superstructure Configuration (Case B)

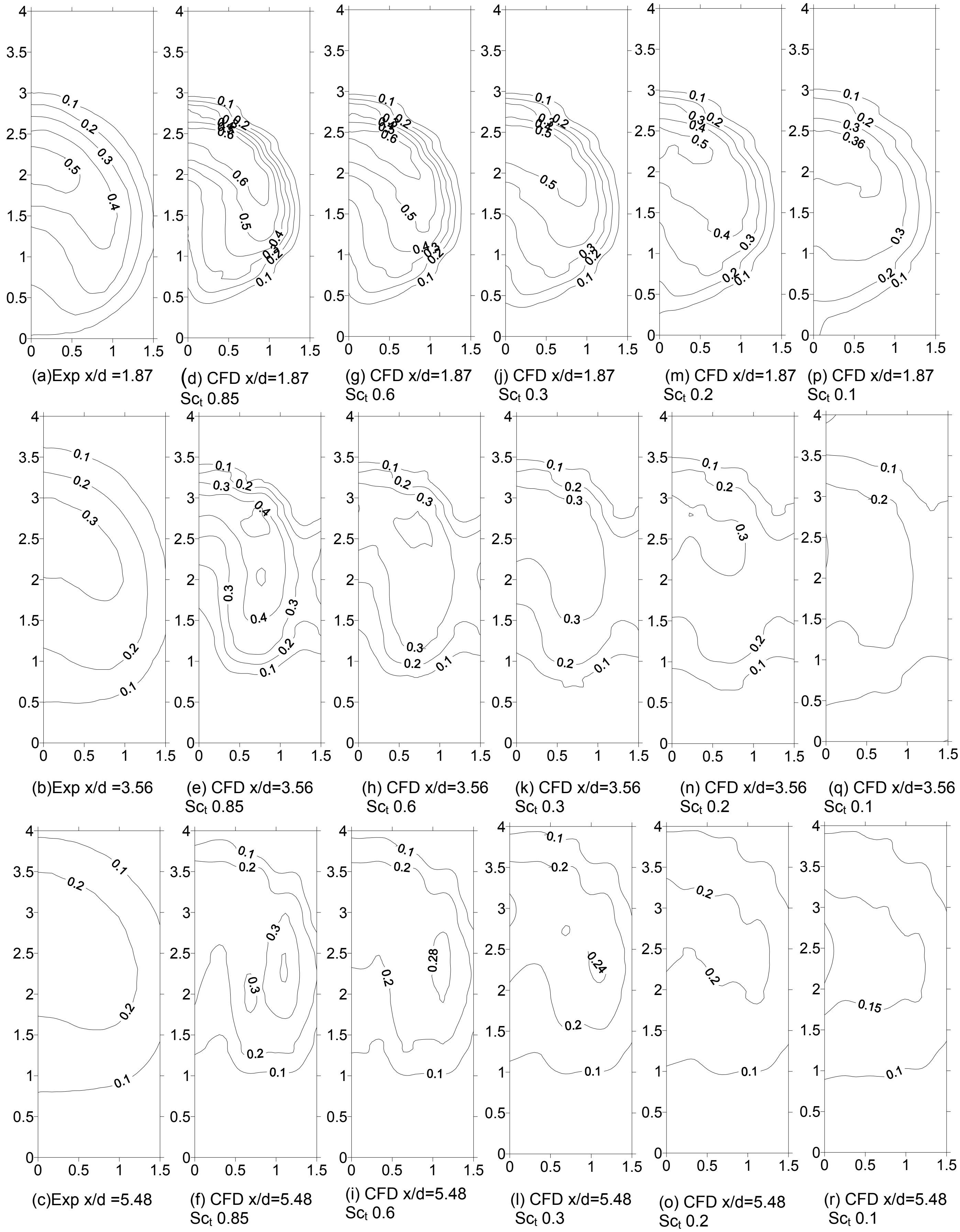

Figure 5: Comparison of iso-temperature contours between experimental results [15] and CFD prediction for various Sct for three planes at M=2.0

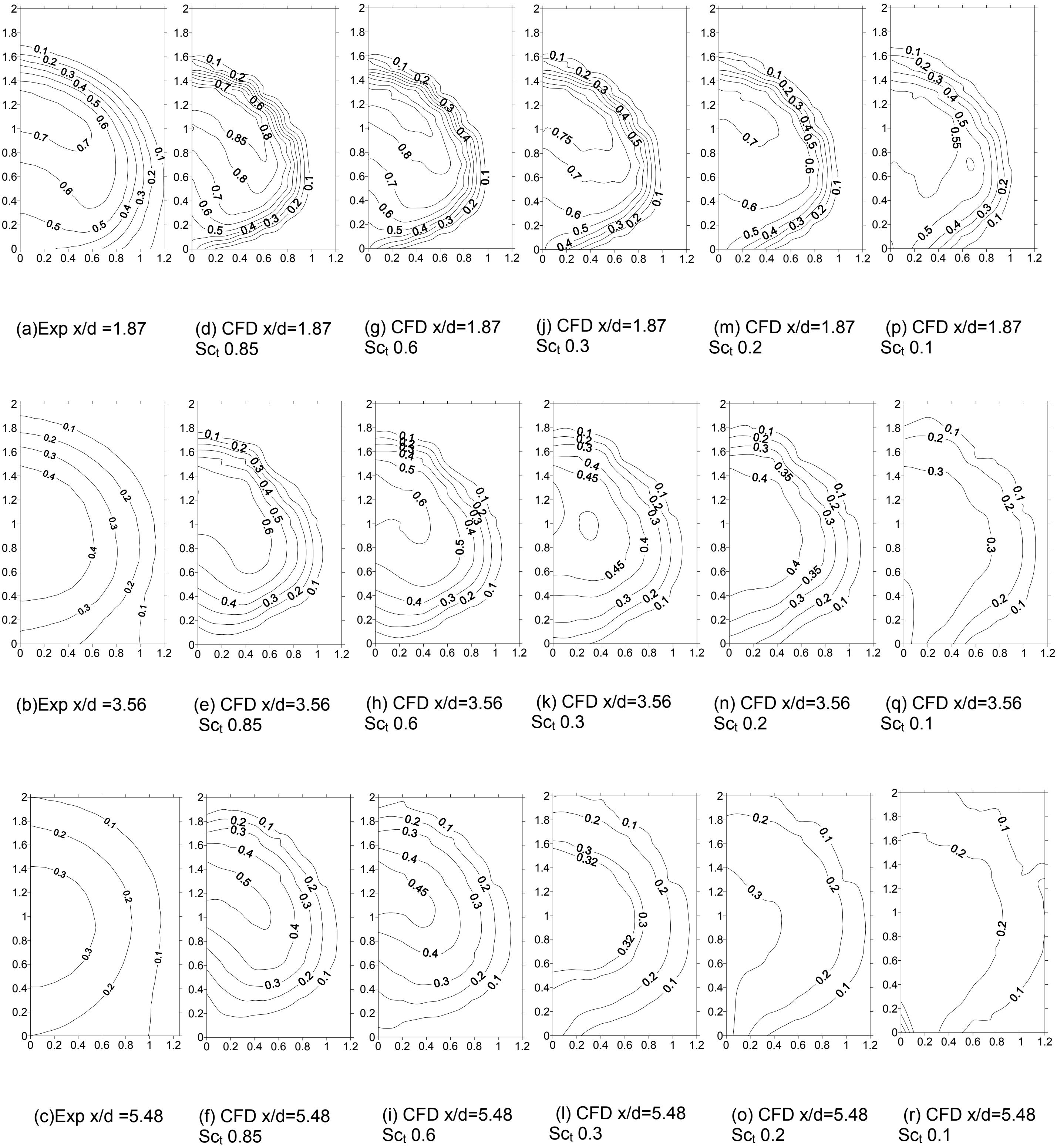

Figure 6: Comparison of iso-temperature contours between experimental results [15] and CFD prediction for various Sct for three planes at M=1.0

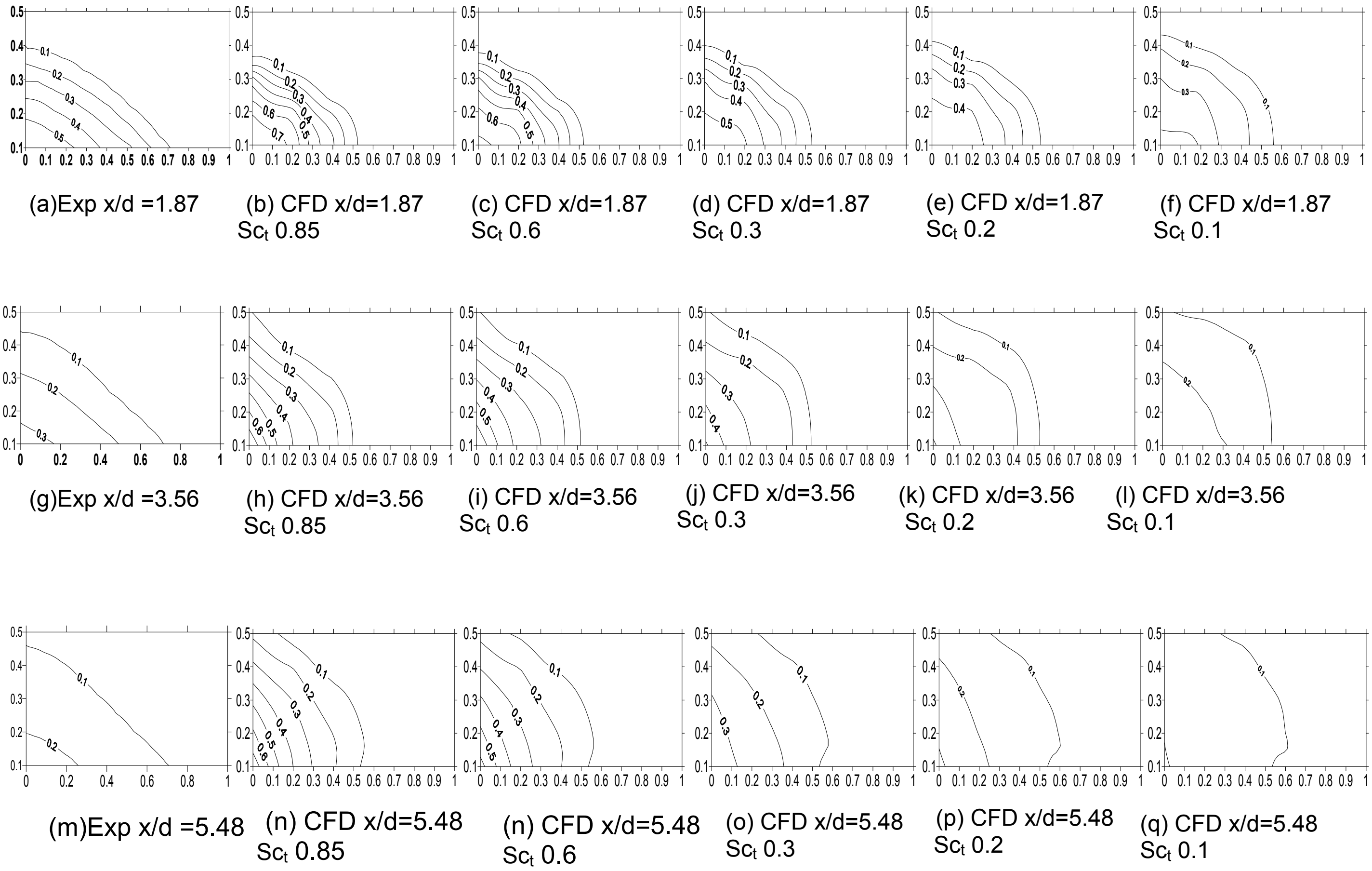

Figure 7: Comparison of iso-temperature contours between experimental results [15] and CFD prediction for various Sct for three planes at M=0.1

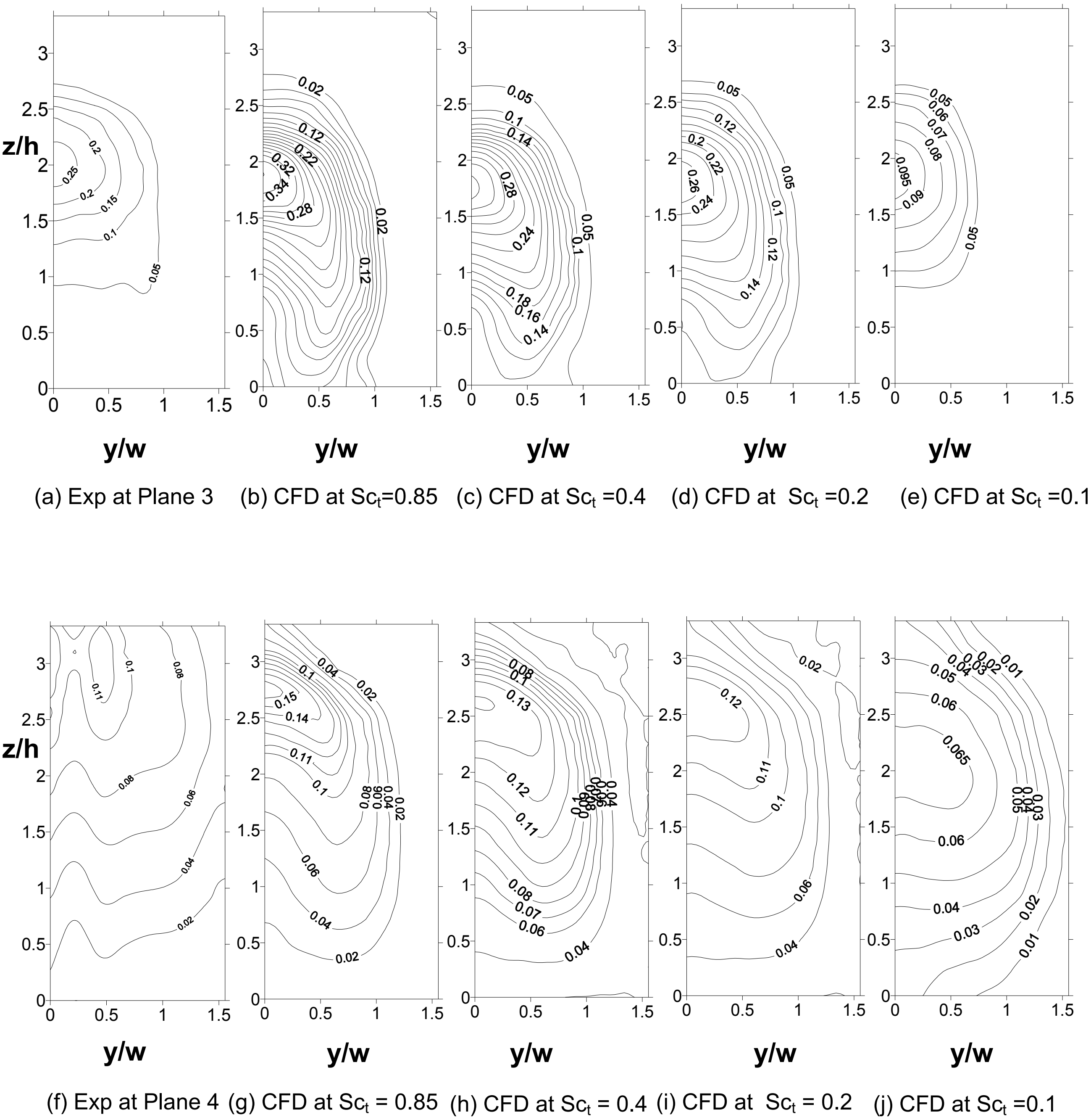

Figure 8: Comparison of iso-temperature contours between Experimental Results[18] and CFD Prediction for various Sc_t for Planes 1 and 2

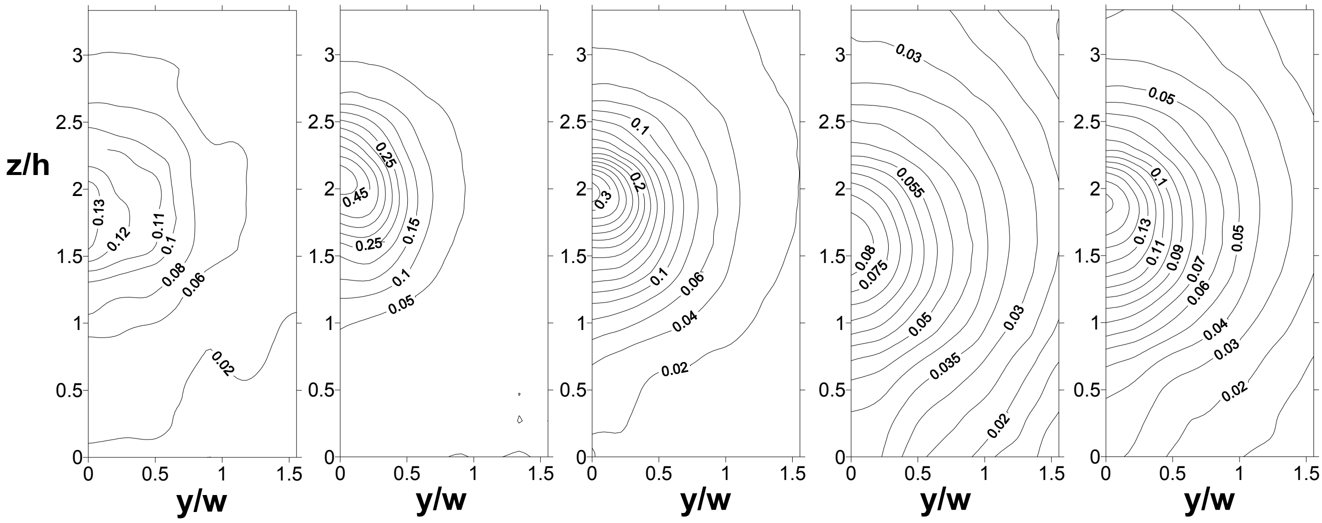

(a) Exp at Plane 8 (b) CFD at Sc_t=0.85 (c) CFD at Sc_t = 0.4 (d) CFD at Sc_t =0.2 (e) CFD at Sc_t = 0.1

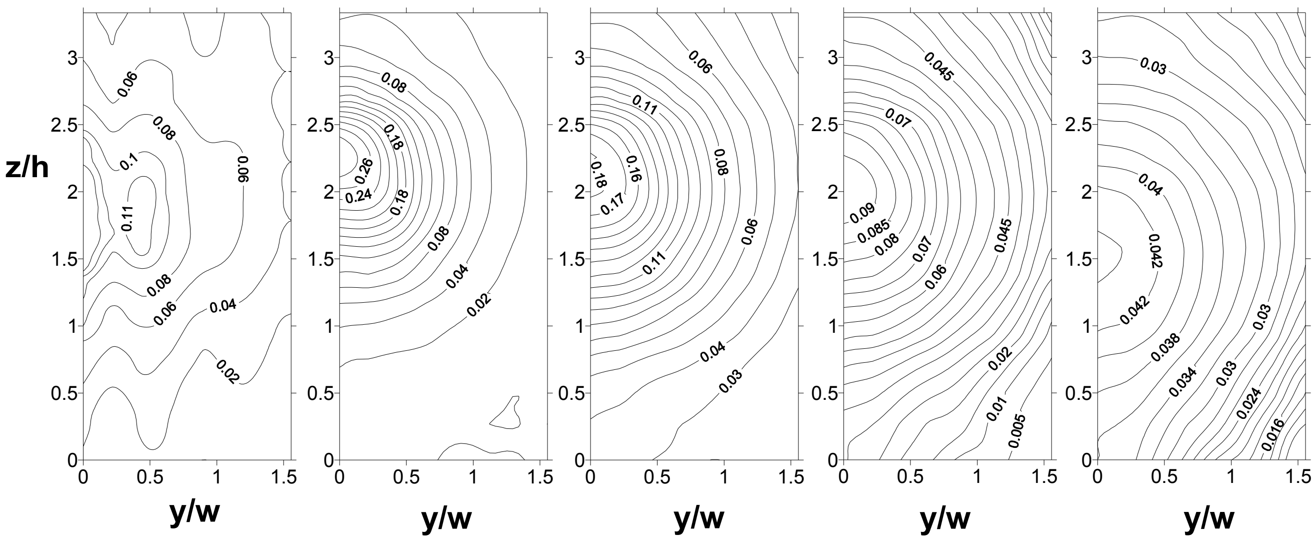

(f) Exp at Plane 9 (g) CFD at Sc_t=0.85 (h) CFD at Sc_t = 0.4 (i) CFD at Sc_t =0.2 (j) CFD at Sc_t = 0.1

Figure 9: Comparison of iso-temperature contours between Experimental Results[18] and CFD Prediction for various Sct for Planes 3 and 4

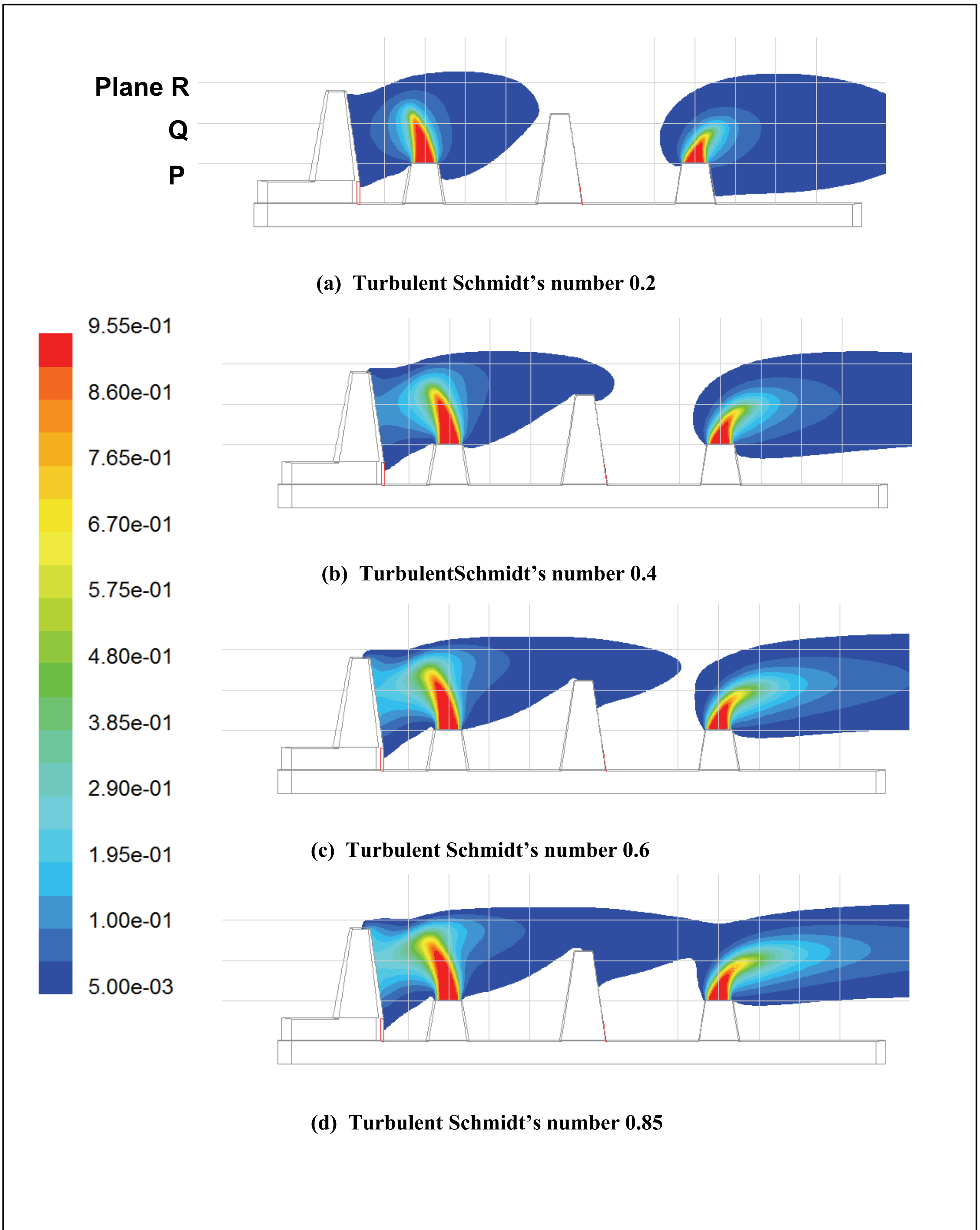

(a) Turbulent Schmidt's number 0.2

(b) TurbulentSchmidt's number 0.4

(c) Turbulent Schmidt's number 0.6

(d) Turbulent Schmidt's number 0.85

Figure 10: Iso temperature plots of θ for centerline plane for various Sct at K = 1, Te=350 K,ψ = 0°, M=1 and Ta=300 K.

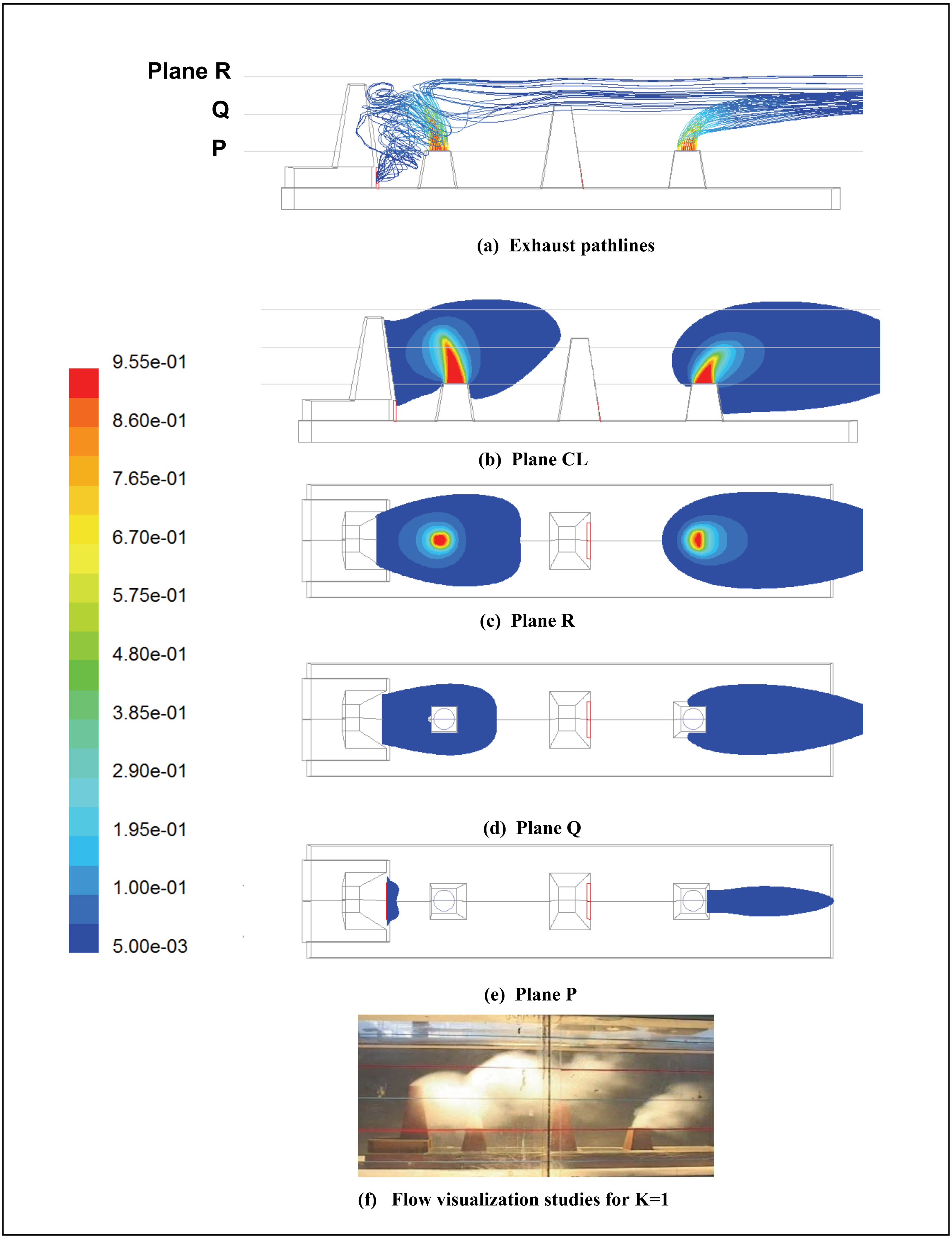

Figure 11: Iso temperature plots of θ for various planes of Model A Sc_t=0.2 at K = 1, Te=350 K, ψ = 0°, M=1 and Ta=300 K

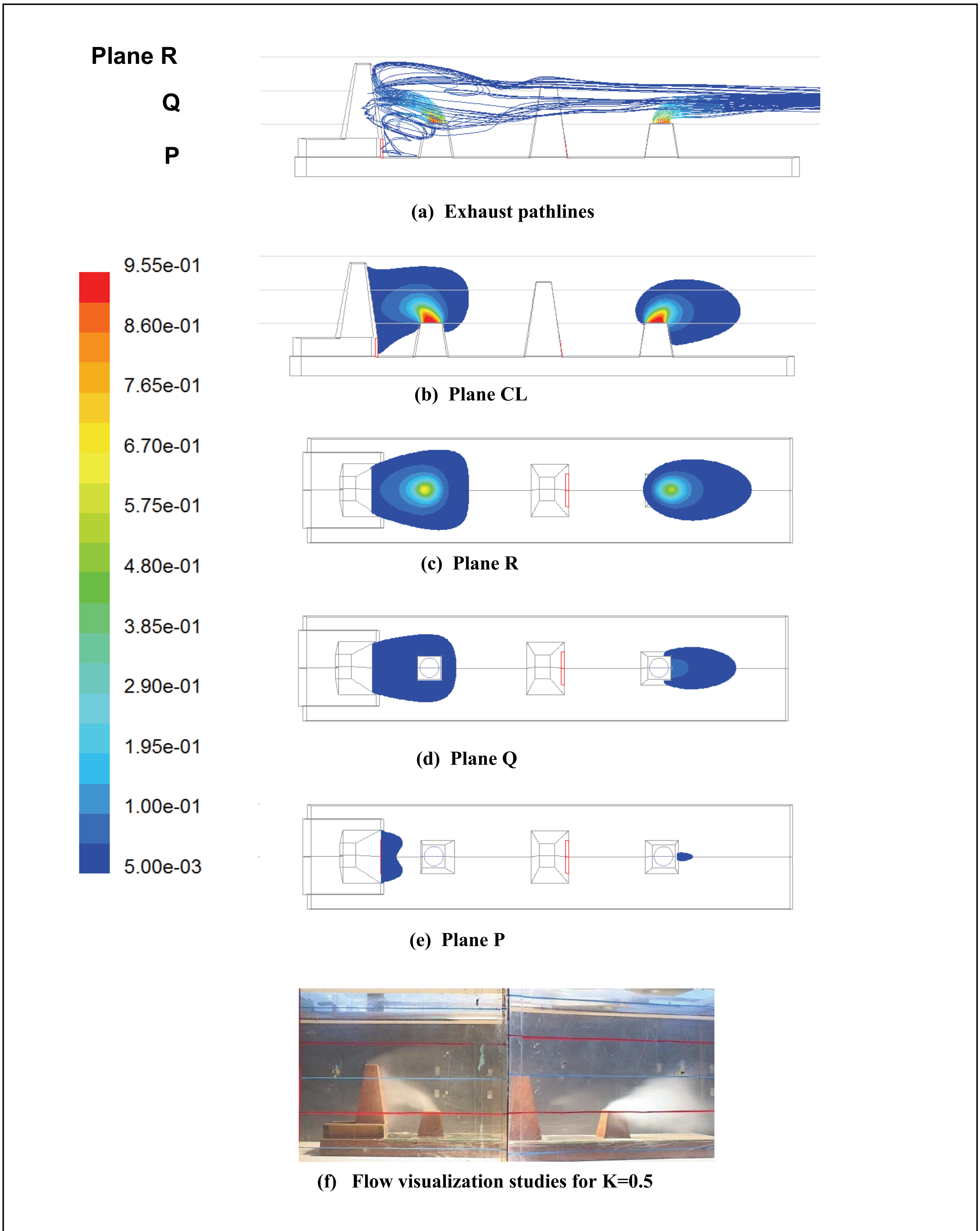

(a) Exhaust pathlines

(b) Plane CL

(c) Plane R

(d) Plane Q

(e) Plane P

(f) Flow visualization studies for K=0.5

Figure 12: Iso temperature plots of θ for various planes of Model A Sc_t =0.2 at K = 0.5, Te=350 K,ψ = 0°, M=1 and Ta=300 K

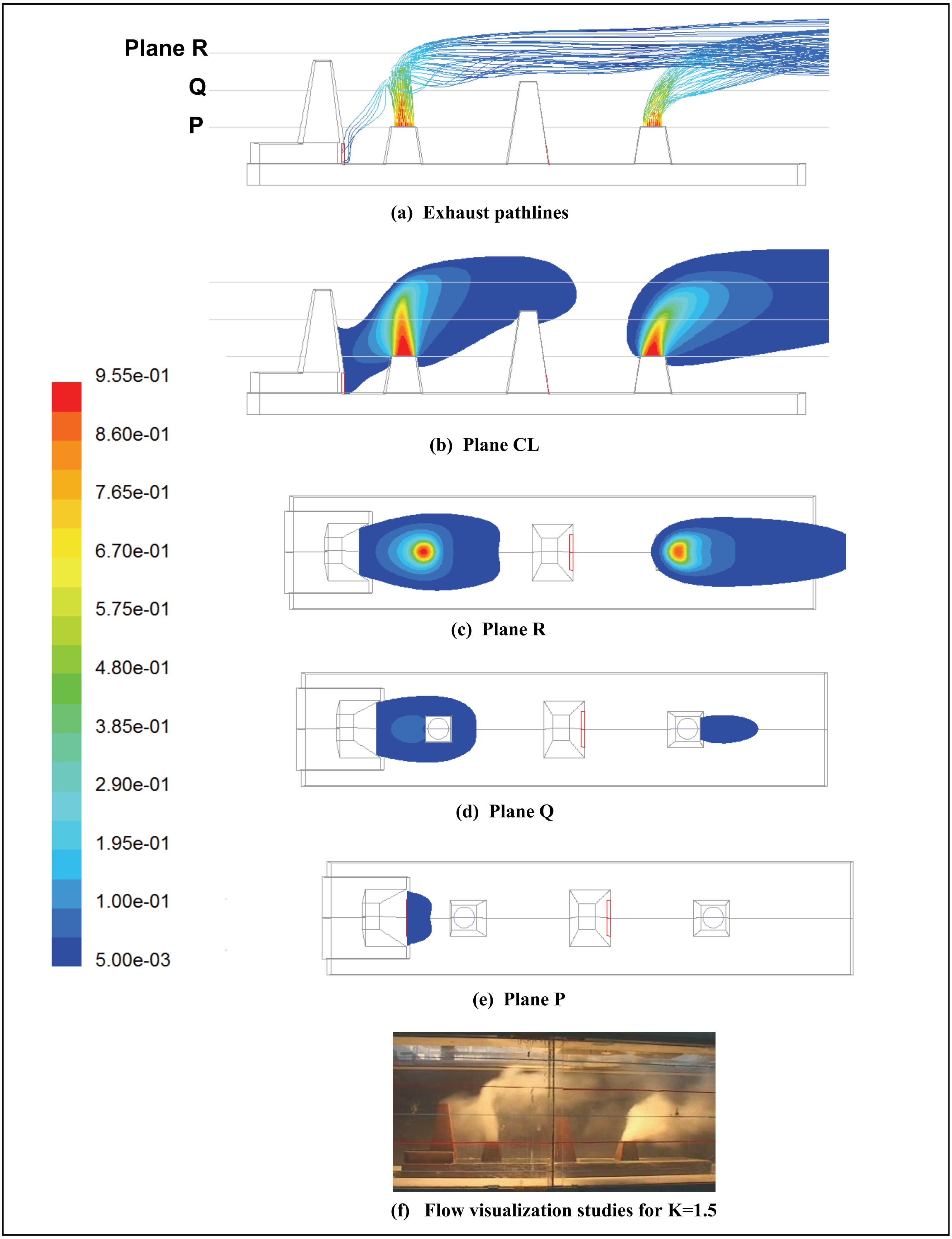

Figure 13: Iso temperature plots of θ for various planes of Model A Sc_t =0.2 at K = 1.5, Te=350 K,ψ = 0°, M=1 and Ta=300 K

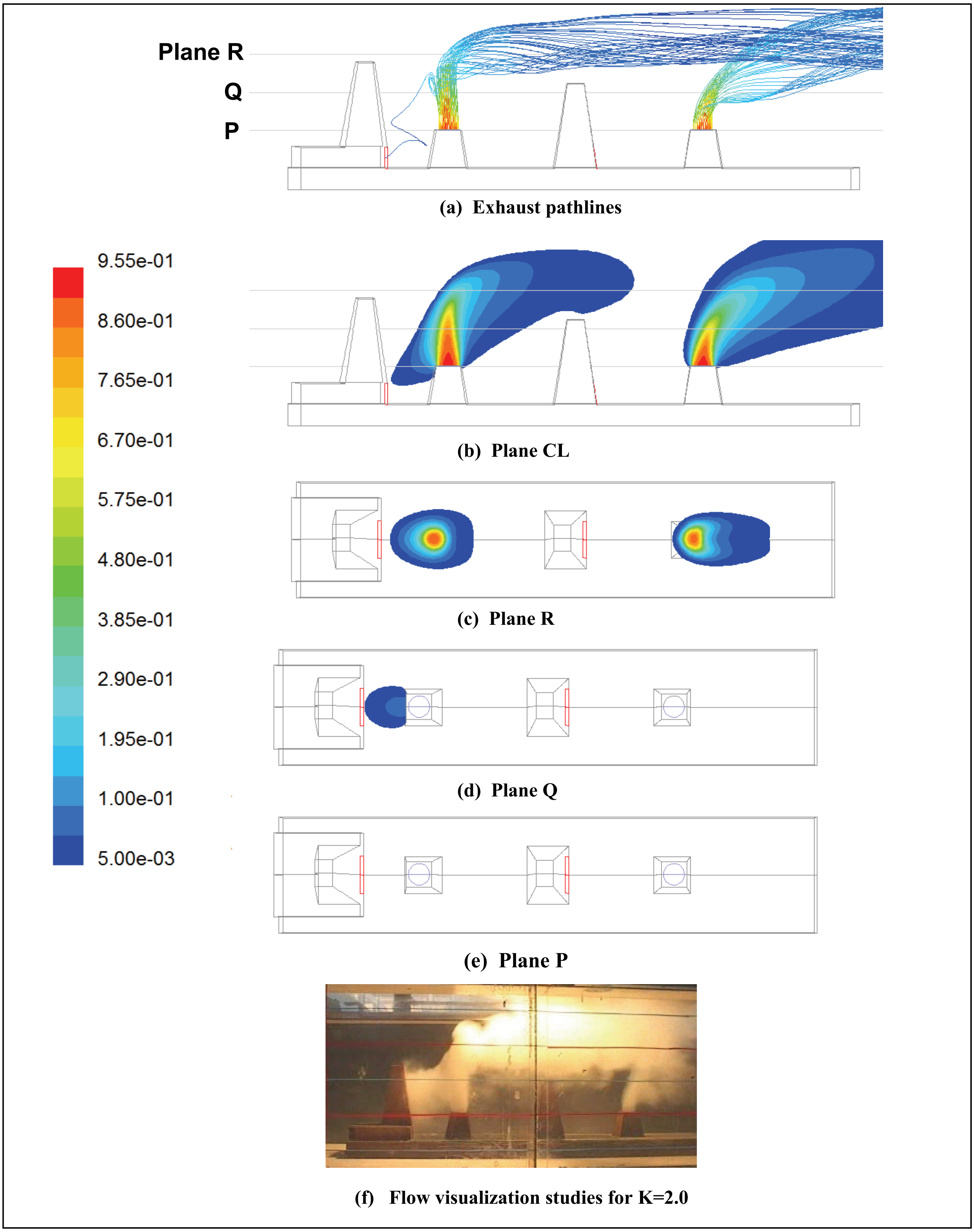

Figure 14: Iso temperature plots of θ for various planes of Model A for Sc_t =0.2 at K = 2.0, Te=350 K,ψ = 0°, M=1 and Ta=300 K